Physics and chemistry of interstellar ice

Guss, K.M.R.

Citation

Guss, K. M. R. (2013, March 26). *Physics and chemistry of interstellar ice*. Retrieved from https://hdl.handle.net/1887/20666

Author: Guss (née Isokoski), Karoliina Marja-Riita
Title: Physics and chemistry of interstellar ice
Issue Date: 2013-03-26

Chapter III

MORPHOLOGY OF POROUS AMORPHOUS SOLID WATER AND CO_2 CONTAINING ICES

Morphology of porous amorphous solid water and CO_2 containing ices
K. Isokoski, J.-B. Bossa, K. and H. Linnartz
Astronomy & Astrophysics, 2013, to be submitted

Abstract

This article aims to characterize the morphological changes in porous amorphous solid water (ASW) upon thermal annealing in pure form and mixed with CO_2. We use laser optical interference to derive refractive indices for H_2O, CO_2, and binary H_2O-CO_2 ice at different temperatures. The morphological changes during thermal annealing are inferred by a combination of optical interference and FTIR spectroscopy. Optical interference is used to monitor the ice thickness in real time, while FTIR spectroscopy gives information about the changes in molecular environment. The refractive index and thermal collapse of pure ASW show a non-linear temperature dependence. The intrinsic $I_{hda} \rightarrow I_{lda}$ phase transition in ASW is visible as discontinuity in thermal collapse at 38–70 K. The structure of porous ASW is not fully compacted by thermal annealing. Depending on the growth temperature, the residual porosity after annealing to 120 K is around 20 %. Large cavities remain in the ice throughout the solid phase, not observable through infrared spectroscopy.

The presence of CO_2 in porous ASW influences the ice morphology throughout the solid phase. Significant morphological changes occur around the $I_{hda} \rightarrow I_{lda}$ phase transition. CO_2 segregation is observed at 70-80 K, and its efficiency depends on the ice morphology. A high initial porosity leads to a higher extent of CO_2 segregation. The morphology of H_2O containing ices is dominated by both intrinsic structure of ASW as well as porosity. Both influence the dynamics in low-temperature ices, and may have significant consequences on the solid state chemistry in interstellar ices. The initial porosity of the ice determines its structural evolution throughout the solid phase until ice evaporation. H_2O rich ices formed by vapor deposition on cold interstellar dust grains may contain large cavities that persist over a large temperature range, and affect the catalytic potential of the ice as well as the trapping of gases. The presence of CO_2 rich porous ASW in the ISM may have interesting consequences for ice dynamics. The growth conditions influence the morphology of mixed ices, which is retained at higher temperatures affecting astronomically relevant processes such as ice segregation.

3.1 Introduction

Amorphous solid water (ASW) is the main component of interstellar and cometary ices (Whittet et al. 1998, Boogert et al. 2008). It provides a matrix environment for other species, such as carbon dioxide CO_2, adsorbed or formed on the ice surface. ASW is able to support a highly porous structure containing large scale internal cavities. The internal surface area of porous ASW ice can be hundreds of m^2/g (Mayer & Pletzer 1986, Bar-Nun et al. 1987), making ice morphology an important factor for interstellar chemical processes relying on surface accessibility. Porous ice provides large effective surface areas for adsorption of atoms and molecules, catalysis of chemical reactions, and further retention of the involved species. Large quantities of molecules can be stored inside pores and later thermally released (Collings et al. 2003, Raut et al. 2007b).

The exact morphology of ice in the interstellar medium (ISM) is still under debate.

The available remote observations of H_2O rich ices (Keane et al. 2001, Gibb et al. 2004) indicate a compact (non-porous) structure inferred from the absence of the dangling OH feature around 2.7 μm (Rowland & Devlin 1991, Rowland et al. 1991, Buch & Devlin 1991). In the laboratory, H_2O formation through surface reactions indeed seems to produce compact ASW (Oba et al. 2009). However, H_2O condensation from the gas phase onto cold surfaces has been shown to lead to porous ASW (Dohnálek et al. 2003). Formation of porous grain mantles in the ISM through vapor deposition of H_2O is expected to occur in dark clouds (Williams et al. 1992, Papoular 2005), but may also be relevant in shock regions and protostellar outflows, where the sputtering of frozen water molecules from grain mantles redistributes ice on the remaining cold surfaces. Vapor deposition from the gas phase may be also relevant in protoplanetary disks where material is transported back and forth across the snow line (*e.g.*, Wooden et al. 2005).

Energetic processing in the ISM is expected to reduce the porosity of ASW. The compaction of porous ASW has been experimentally demonstrated to be driven by cosmic rays and UV photons (Palumbo 2006, Palumbo et al. 2010, Raut et al. 2008), as well as by thermal processing (Bar-Nun & Owen 1998, Bossa et al. 2012). Many of the observations covering the 2.7 μm region are targeting embedded sources with processed ices, where porosity may have decreased (Whittet et al. 1998, Boogert et al. 2008). Given the diversity of astronomical ice environments, the absence of porous ASW is therefore not conclusive (Kouchi & Yamamoto 1995, Gálvez et al. 2010).

The transformation from porous to compact ice may have interesting consequences for the chemistry in interstellar ice. Pore collapse at low temperatures drive diffusion limited recombination of radicals trapped in interstellar ices. In UV irradiated interstellar ice analogs (Schutte 1988), the observed low-temperature chemical evolution has been attributed to a structural phase transition in the ice between 38 and 68 K (Jenniskens & Blake 1994). Spectral changes, however, are observed prior to this and therefore cannot be directly due to the phase transition only. In our previous work, we showed that the thermally induced collapse of porous ASW begins at temperatures as low as 20 K and continues gradually throughout the amorphous phase (Bossa et al. 2012). Low-temperature pore collapse may thus be responsible for chemical evolution at low temperatures. Porosity of interstellar ice may be also relevant in planet formation. It has been suggested that porous ice mantles facilitate the coagulation of dust grains in the process of forming larger solar system bodies (Krijt private communication).

The morphology of ASW grown in the laboratory depends on experimental conditions such as temperature, growth rate and directionality of H_2O molecules landing on the ice surface (Berland et al. 1995, Westley et al. 1998, Stevenson et al. 1999, Kimmel et al. 2001b, Dohnálek et al. 2003). Omnidirectional background deposition onto a cold surface leads to highly porous ASW. Monitoring the decrease in porosity during energetic processing is typically done through IR spectroscopy, where compaction is derived from the decrease in intensity of the dangling OH bonds (*e.g.*, Palumbo 2006), or by gas absorption probing the available pore volume (*e.g.*, Raut et al. 2007b). In Bossa et al. (2012), we employed optical interference to monitor the porous ASW thickness during thermal annealing. This technique is commonly used to monitor ice growth during the preparation of interstellar ice analogs.

In this paper, we extend the work in Bossa et al. (2012) and study in more detail the thermally induced changes in the morphology of astronomically relevant ices. We focus on porous ASW, pure CO_2 ice and the H_2O-CO_2 (4:1) binary ice mixture. CO_2 is the most common impurity in interstellar H_2O ice with ratios as highas ~30 % and is therefore important for its morphology. We use optical interference to derive the specific refractive indices of different ice samples. Following instrumental improvements we are now more sensitive to changes in ice thickness, in particular during thermal annealing.

3.2 Experimental methods

3.2.1 Experimental setup

The experimental setup was originally described by Gerakines et al. (1995) and has been adapted to the configuration described here (Fig. 3.1). A stainless steel chamber is evacuated by a turbomolecular pump (Pfeiffer TPH 170) and a mechanical pump (Edwards E2M8) equipped with an oil mist filter to a base pressure of 2×10^{-7} Torr at room temperature. Ice samples are grown on a silicon substrate located in the center of the chamber. The substrate is mounted on a closed-cycle helium cryostat that, in conjunction with resistive heating, allows for temperature control from 17 to 300 K with a precision of 0.1 K.

Samples are prepared in a glass bulb by standard manometric techniques using an external gas mixing line with a base pressure of 1×10^{-5} mbar. We use milli-Q grade H_2O that is further purified by three freeze-pump-thaw cycles. CO_2 (Praxair, 99.998 % purity) is used without further purification. Each sample is prepared at a total pressure of 20 mbar. The H_2O-CO_2 (4:1) gas sample is prepared by placing H_2O vapor (16 mbar) into a pre-evacuated bulb. CO_2 is subsequently introduced into the bulb by a rapid gas expansion from an external volume, pre-filled to give the desired CO_2 partial pressure (4 mbar). The bulb valve is closed immediately after expansion to prevent diffusion of H_2O into the external volume. Gas samples with two components are prepared ~20 h prior to deposition. This allows the gas mixture to equilibrate with the bulb walls, ensuring a reproducible ice composition.

Samples are admitted into the vacuum chamber through a needle valve. The ices are grown by *background deposition* where the gas inlet is directed away from the substrate. This method allows the molecules to impinge on the surface with random trajectories, producing a porous ice structure (Stevenson et al. 1999, Dohnálek et al. 2003). The pressure in the chamber during deposition is set to $1.0 \pm 0.1 \times 10^{-5}$ Torr. We use a gas reservoir with a large volume (2 L) to ensure a constant deposition rate. The deposited ice samples are thermally annealed at a constant rate of 2.0 K min^{-1} until desorption.

3.2.2 Optical interference

The refractive indices of the ice samples as well as their thickness throughout the experiment (deposition and thermal annealing) are derived using optical interference. The interference of coherent light reflecting off the two interfaces of a thin film depends on the

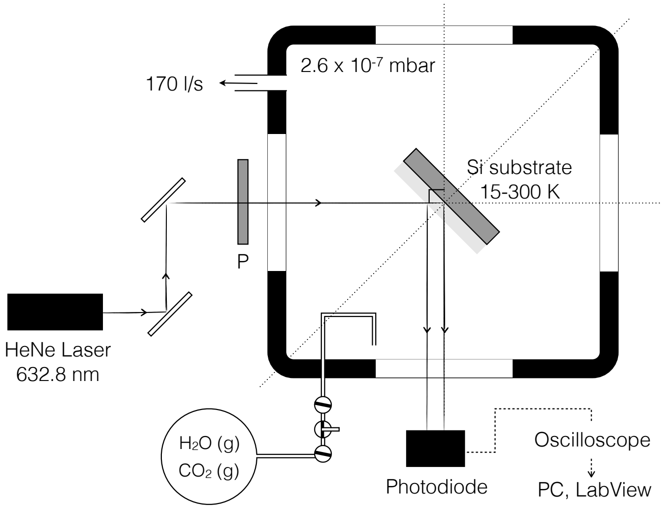

Figure 3.1 – Schematic drawing of the experimental setup used to measure thin-film interference in interstellar ice analogs. P = linear polarizer.

optical properties of the media involved, as well as the thickness of the film. We employ a linearly polarized, intensity stabilized HeNe laser (Thorlabs HRS015). An additional polarizer is placed in the beam path admitting only s-polarized light, perpendicular with respect to the plane of incidence. The laser beam strikes the substrate surface at an incident angle of 45°. For the purpose of the interference experiment a porous ice film with nm-scale surface features presents an effectively flat surface to the laser beam (spot size 2 mm). The reflected light is collected at a photodiode (Thorlabs PDA36A) and digitized by an oscilloscope (Textronix TDS 2022B). The photodiode signal together with time and substrate temperature from the (Lakeshore 330) temperature controller is recorded using the LabVIEW 8.6 software package (National Instruments).

For a surface with a three-phase structure, as depicted in Fig. 3.2, the total reflection coefficient R can be described by Eq. 3.1 (Westley et al. 1998, Dohnálek et al. 2003):

$$R = \frac{r_{01} + r_{12}e^{-i2\beta}}{1 + r_{01}r_{12}e^{-i2\beta}}; \quad \text{with} \tag{3.1}$$

$$\beta = \frac{2\pi d}{\lambda} \times n_1 \cos\theta_1$$

where r_{01} and r_{12} are the Fresnel reflection coefficients for the vacuum/ice and ice/substrate surface interfaces, d is the thickness of the ice, λ is the wavelength of the laser (632.991 nm) and n_1 is the refractive index of the ice. θ_1 is the angle of refraction, derived from the angle of incidence θ_0 through $n_0 \sin\theta_0 = n_1 \sin\theta_1$ (Snell's law). For s-polarized light the

Fresnel reflection coefficients can be written as:

$$r_{01s} = \frac{n_0 \cos\theta_0 - n_1 \cos\theta_1}{n_0 \cos\theta_0 + n_1 \cos\theta_1} \tag{3.2}$$

and

$$r_{12s} = \frac{n_1 \cos\theta_1 - n_2 \cos\theta_2}{n_1 \cos\theta_1 + n_2 \cos\theta_2} \tag{3.3}$$

where n_0 and n_2 are the refractive indices of vacuum and substrate. We use constant refractive indices $n_0 = 1$ for vacuum and $n_2 = 3.85 - 0.07i$ for the Si substrate (Mottier & Valette 1981).

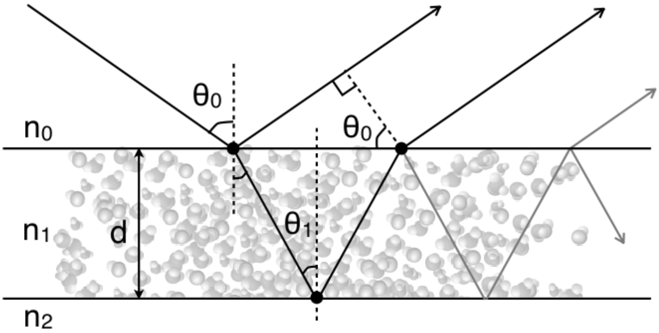

Figure 3.2 – Optical interference in a three-phase (vacuum/ice/substrate) structure. Light incident on the surface interface between two media partially reflects from and partially refracts into the layer, depending on the Fresnel reflection coefficients (r_{01} and r_{12}). The difference in optical path length leads to a phase shift and an alternating constructive and destructive interference during layer growth. The intensity of the sum reflection depends on the refractive indices (n_0, n_1 and n_2) and film thickness (d).

We relate the experimentally measurable photodiode signal (S) to the reflected intensity $|R|^2$ through an empirical scaling factor α, which allows us to correlate S with n_1 and d (Eq. 3.4).

$$S = \alpha \times \left| \frac{r_{01} + r_{12} e^{-i2\beta}}{1 + r_{01} r_{12} e^{-i2\beta}} \right|^2 \tag{3.4}$$

The refractive indices of ice samples for different temperatures are determined by fitting Eq. 3.4 to the photodiode signal during ice growth (Eq. 3.5).

$$S(t) = \alpha \times \left| \frac{r_{01}(n_1) + r_{12}(n_1) e^{-i2\beta(t)}}{1 + r_{01}(n_1)\, r_{12}(n_1) e^{-i2\beta(t)}} \right|^2 \tag{3.5}$$

The thickness d, contained in the β term, is constrained by a linear equation corresponding to a constant growth rate (Eq. 3.6):

Table 3.1 – IR band strengths (A_i) of H_2O and CO_2 stretching modes in pure ices at 14 K.

Mode	Band position [cm^{-1}]	A$_i$ (14 K) [cm molecules^{-1}]	Ref.
H_2O, O–H stretch	3280	2.0E-16	(1)
CO_2, ^{13}C=O (ν_3) stretch	2283	7.8E-17	(2)

References: (1) Hagen (1981); (2) Gerakines et al. (1995)

$$d(t) = \gamma t \tag{3.6}$$

where γ is a constant corresponding to the deposition rate in nm s^{-1}. The decrease of the deposition rate in (Bossa et al. 2012) is here avoided by doubling the volume of the sample reservoir. In the fitting procedure α, γ and n_1 are allowed to vary freely.

We assume that the refractive indices obtained for ices deposited at a particular temperature, are applicable to ice which has been thermally annealed to that temperature. The ice thickness during thermal annealing $d(T)$ can then be derived by finding the closest root (d) to the initial ice thickness that satisfies Eq. 3.7:

$$|R(d,T)|^2 - |R(d_0,T_0)|^2 = 0 \tag{3.7}$$

where $|R(d,T)|^2$ is the reflected intensity at temperature T and $|R(d_0,T_0)|^2$ is the reflected intensity in the beginning of the thermal annealing.

3.2.3 IR spectroscopy

Infrared (IR) spectra are recorded with a Fourier transform infrared spectrometer (Varian 670-IR FTIR) in transmission between 4000 and 400 cm^{-1} with a resolution of 1 cm^{-1}. A total of 256 interferograms are averaged to improve the S/N ratio. Background spectra are acquired at 17 K prior to sample deposition. At annealed temperatures, the ice samples are allowed to relax for 5 min before recording the spectrum.

The column density of molecules in the ice, N (in molecules cm^{-2}), is derived from IR spectra by Eq. 3.8 (Gerakines et al. 1995):

$$N = \frac{\ln 10 \times \int A \, d\bar{\nu}}{A_i} \times \cos\theta \tag{3.8}$$

where $\int A \, d\bar{\nu}$ is the integrated intensity of a particular absorption band and A_i is the band strength in cm molecules^{-1}. The last term in Eq. 3.8 corrects the overestimation of N resulting from the non-orthogonal orientation of the IR beam and the ice sample (Bennett et al. 2004). Table 3.1 lists the band strengths for the fundamental vibrational modes in pure H_2O and CO_2 ices used here.

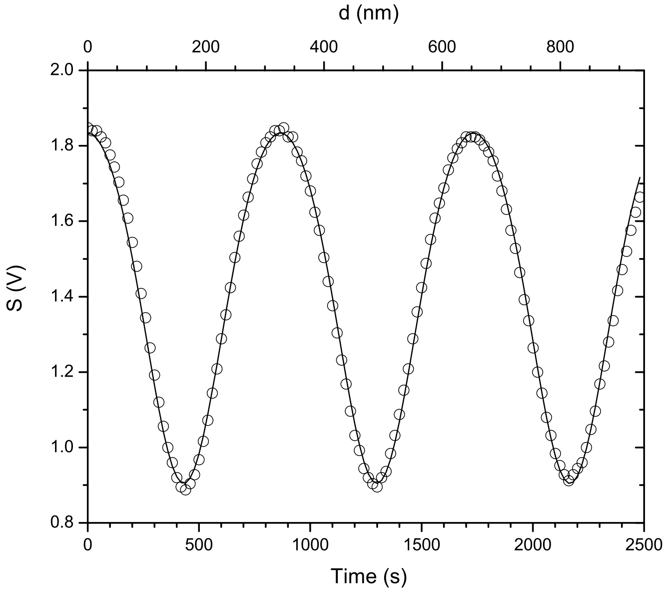

Figure 3.3 – Optical interference signal (S) during deposition of H_2O ice at 17 K (open circles) and fit using Eq. 3.5 (black trace) for the deposition fringe pattern.

3.3 Results

3.3.1 Deposition

Fig. 3.3 shows the interference signal (S) during the deposition of pure H_2O ice at 17 K. All samples are grown at a similar rate, and cycled through ~3 fringes, resulting in a thickness ranging between 0.9 and 1.0 μm. The deposition is stopped towards the top of the rising slope of one of the interference fringes. Changes in the interference signal thus correspond directly to changes in ice thickness, simplifying real-time interpretation of the results. Moreover, as the ice thickness, d, generally decreases during further processing, the dynamic range of the signal is maximized in this setting. The growth rate for H_2O at 17 K is fairly constant throughout the deposition with <5 % variation in the half-period. For all samples, the observed amplitude of the deposition fringes decreases somewhat during the deposition, likely due to an increasing loss of photons through scattering. For H_2O ice deposited at 17 K the decrease in amplitude is 2 % per period. The black trace in Fig. 3.3 shows the fit of Eq. 3.5 to the fringe pattern. The fitted region is determined by the experimentally noted start and end of deposition. The best fit parameters for all studied samples are given in Table 3.2. Fig. 3.4 shows the R^2 (coefficient of determination) plot describing the goodness of the fit for H_2O deposition at 22 K. A single R^2 maximum demonstrates that the fit has a unique solution.

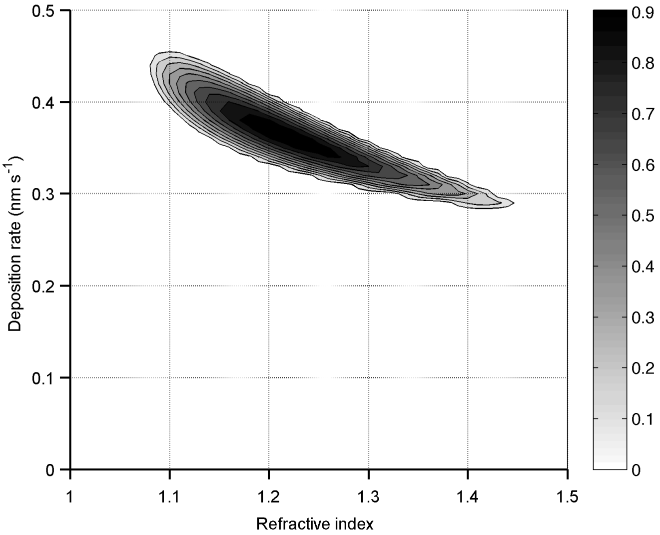

Figure 3.4 – R^2 (coefficient of determination) from the fit using Eq. 3.5 for H_2O deposition fringe pattern at 22 K as a function of refractive index (n_1) and deposition rate (γ), with the scaling factor (α) fixed to an optimized value.

3.3.1.1 Refractive indices

Fig. 3.5 (left panel) shows the refractive indices (n_1) for H_2O, CO_2 and H_2O-CO_2 ices as a function of deposition temperature. For pure H_2O ice, we consider temperatures between 17 and 120 K, where H_2O exists in amorphous form. Under our experimental conditions pure CO_2 ice evaporates between 80 and 90 K, limiting the presented data to 80 K. Mixed H_2O-CO_2 (4:1) ice is also studied at 90 K, where the co-deposited CO_2 does not stick onto the substrate but may influence the morphology of the condensing H_2O ice.

For pure H_2O, n_1 increases from 17 to around 40 K, followed by a decrease towards 60 K. Above 60 K n_1 increases linearly with temperature towards 120 K. For pure CO_2, n_1 increases with temperature from 17 K, reaching a maximum at around 60 K. After 60 K, n_1 decreases towards 80 K. The n_1 obtained for H_2O-CO_2 (4:1) ice resembles that of pure CO_2 ice. Below 40 K, however, n_1 remains higher than for pure CO_2 or H_2O ice. For H_2O-CO_2 ice deposited at 90 K, n_1 remains above the value interpolated for pure H_2Oice, suggesting that the co-deposited CO_2 does indeed influence the morphology of the condensing H_2O ice.

Table 3.2 – Best deposition fringe fit parameters for H_2O, CO_2 and H_2O-CO_2 (4:1) ices. n_1 = refractive index, $1/\alpha$ = inverse scaling factor, γ = deposition rate and R^2 = coefficient of determination.

H_2O

T_d [K]	17	22	30	40	45	50	60	70	80	100	120
n_1	1.199	1.212	1.216	1.22	1.213	1.212	1.209	1.217	1.221	1.239	1.26
$1/\alpha$ [V^{-1}]	3.906	3.959	3.966	3.949	3.88	3.911	3.844	3.864	3.851	3.967	3.809
γ [nm s^{-1}]	0.377	0.365	0.345	0.355	0.37	0.322	0.318	0.291	0.304	0.276	0.247
R^2	0.99606	–	0.99576	0.99626	0.98889	0.99039	0.98829	0.98907	0.97713	0.99216	0.98999

CO_2

T_d [K]	20	30	40	45	50	60	70	80
n_1	1.221	1.257	1.278	1.293	1.315	1.313	1.309	1.272
$1/\alpha$ [V^{-1}]	3.854	3.864	3.809	3.833	3.842	3.79	3.78	3.45
γ [nm s^{-1}]	0.298	0.271	0.213	0.208	0.213	0.191	0.192	0.207
R^2	0.99118	0.98113	0.9861	0.98644	0.98431	0.9392	0.9593	0.93363

H_2O-CO_2 (4:1)

T_d [K]	20	30	40	45	50	60	70	80	90
n_1	1.261	1.271	1.274	1.286	1.295	1.295	1.285	1.269	1.251
$1/\alpha$ [V^{-1}]	3.951	4.009	3.935	3.831	3.856	3.918	3.841	3.736	3.989
γ [nm s^{-1}]	0.352	0.31	0.179	0.197	0.151	0.172	0.199	0.185	0.158
R^2	0.99779	0.99823	0.99416	0.99382	0.98955	0.98553	0.99121	0.98312	0.98364

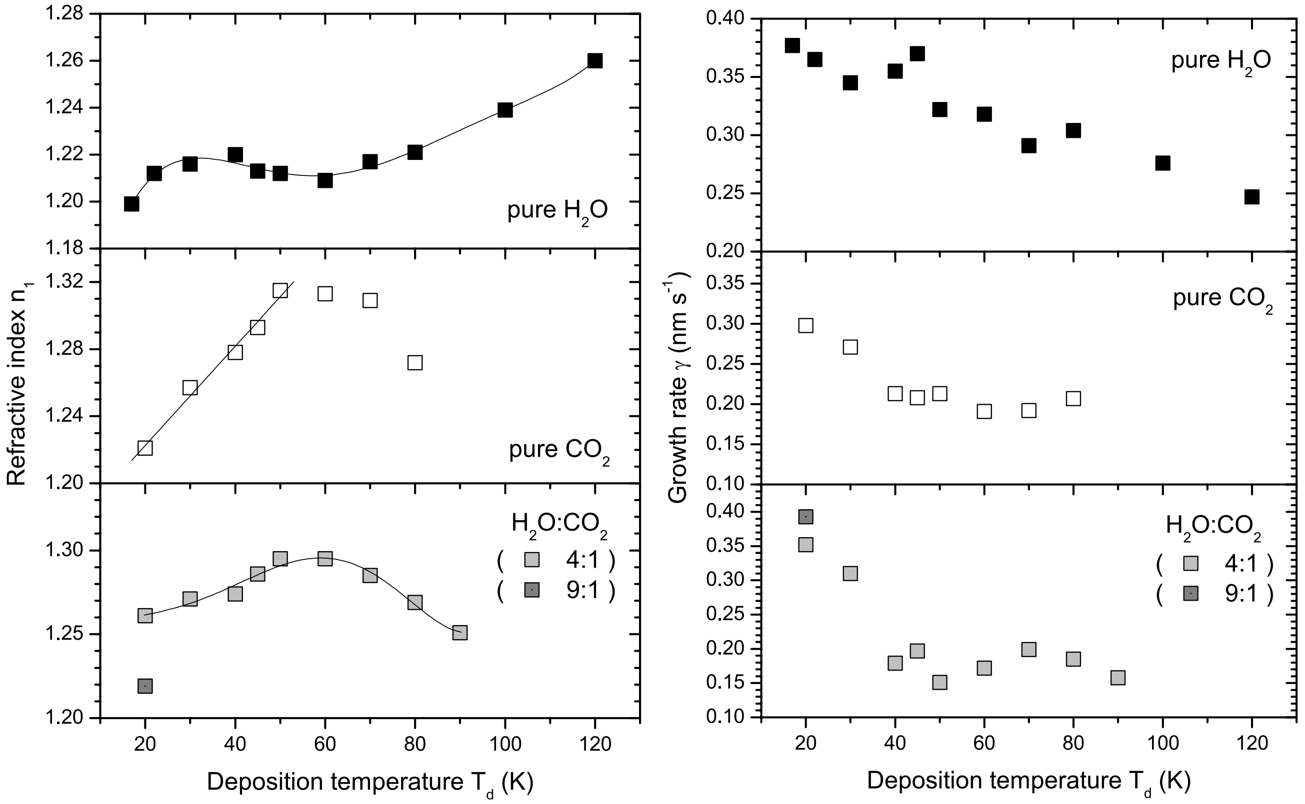

Figure 3.5 – Refractive indices (n_1) (left panel) and growth rates (γ) (right panel) for H_2O, CO_2, and H_2O-CO_2 ices as a function of deposition temperatures. The 5th order polynomial and linear fits of $n(T)$ are shown as black traces in the left panel (see Sect. 3.3.3).

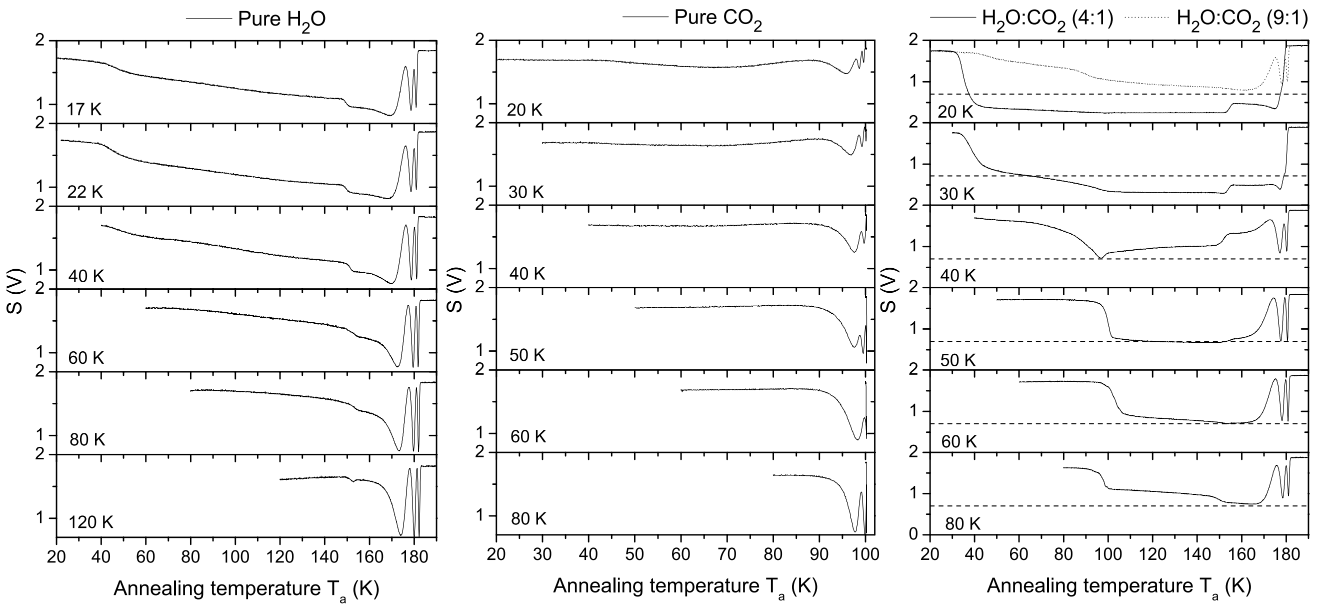

Figure 3.6 – Interference signal (S) during thermal annealing of pure H_2O ice (left panel), pure CO_2 ice (middle panel) and H_2O-CO_2binary ice mixture (right panel). The different traces correspond to samples deposited at different temperatures as indicated in each panel. A dashed rule is drawn in the right panel at $S = 0.7$ V corresponding to the approximate level of full destructive interference during the deposition of H_2O-CO_2 (4:1) ices.

3.3.1.2 Growth rates

Fig. 3.5 (right panel) shows the growth rates (γ) for H_2O, CO_2 and H_2O-CO_2 ices as a function of deposition temperature. Assuming that the sticking coefficient does not significantly change with temperature, γ can be inversely correlated with the density of the growing ice: higher density requires more molecules per unit volume, which for a constant molecular deposition rate manifests itself as a slower ice growth rate. However, variations in the growth rate smaller than 10 % cannot be assigned to density effects because of the uncertainty in the experimentally set deposition pressure. The growth rate of pure H_2O ice generally decreases with temperature, suggesting an increasing density. At around 40 K, however, the density is lower than for adjacent points. For pure CO_2 ice, γ decreases with temperature reaching a minimum around 60 K, before increasing towards 80 K. The density of CO_2 ice is thus highest for ice at ~60 K. This is consistent with the found n_1, which reaches a maximum at about 60 K. For H_2O-CO_2 (4:1) ice the decrease in γ and increase in density is dramatic between 30 and 40 K. Indeed, as will be shown in Sect. 3.3.2, ices grown at 20 and 30 K exhibit qualitatively different behavior upon thermal annealing when compared to ice grown at 40 K.

3.3.2 Thermal annealing

Fig. 3.6 shows the interference signal (S) during thermal annealing of H_2O, CO_2 and H_2O-CO_2 ices deposited at different temperatures. The starting point here coincides with the end of deposition in Fig. 3.3. For the H_2O sample deposited at 17 K (top panel), the signal decreases gradually as the temperature increases. A phase of faster decrease is observed between 40 and 50 K, after which the slow gradual decrease continues. The signal drops quickly at around 150 K corresponding to the temperature region where H_2O crystallization takes place. Above 160 K H_2O starts to thermally desorb. During desorption, the signal cycles back through the interference fringes as the ice becomes thinner. Qualitatively similar behavior is seen for ices grown at higher temperatures (20-120 K). However, the amplitude of the desorption fringe pattern is visibly smaller for ices grown at a lower temperature.

For pure CO_2 ice, which crystallizes between 35 and 50 K (Falk 1987), the interference signal remains relatively constant until 90 K. For CO_2 grown below 50 K, a slight decrease in signal is observed above 45 K. As is the case for H_2O, the amplitude of the desorption fringe pattern for pure CO_2 ice appears smaller for ices grown at low temperature. For CO_2, however, the fringes resulting from thermal annealing cannot be fully resolved due to fast desorption.

For H_2O-CO_2 (4:1) ice, there are clear qualitative differences between ices deposited at different temperatures. For ices deposited at 50, 60 and 80 K (bottom three panels of Fig. 3.6), the signal is stable until 90-95 K after which it drops and reaches a phase of slow decrease around 110 K. As the ice temperature is further increased, the signal gradually approaches the desorption fringe pattern. For ices deposited at 20 and 30 K (top two panels of Fig. 3.6), the signal decreases abruptly after 30 K and continues to dive below the level of complete destructive interference (marked with a dashed horizontal rule). A value of S smaller than that for complete destructive interference can only be due to loss of photons – likely due to a significant change in the optical quality of the sample. For H_2O-CO_2 (4:1) ice deposited at 40 K, the above is not observed; the signal decreases exponentially towards 100 K until it reaches the fringe turning point and continues to increase again. A sudden change in S around 150 K, similar to pure H_2O samples, is visible for mixed ices, although at somewhat varying temperatures. Thermal annealing of H_2O-CO_2 ice with a higher mixing ratio (9:1) deposited at 17 K, does not exhibit this anomalous behavior (Fig. 3.6). The signal decrease follows that of pure H_2O, with a drop between 40 and 50 K. Another drop in signal is observed around 80–90 K, similar to the H_2O-CO_2 (4:1) samples deposited at higher temperatures, and coincident with the desorption temperature of pure CO_2.

3.3.3 Thickness

In order to derive the degree of thermal collapse of ices, we use Eq. 3.7 to calculate the thickness (d) of the ice at a particular temperature. $n_1(T)$ is obtained by fitting 5th order polynomial (H_2O and H_2O-CO_2) or linear (CO_2) equations to the datasets in Fig. 3.5. For pure CO_2 ice, the thickness is derived between 20 and 50 K only, as possible changes in the surface reflectance after crystallization prohibit interpretation above 50 K. The same reasoning limits the analysis of the H_2O ice data to 120 K.

Fig. 3.7 shows the thermal evolution of the thickness in H_2O, CO_2, and H_2O-CO_2 (4:1) ices deposited at 22, 20 and 40 K, respectively. Pure H_2O ice shows periods of rapid and slow collapse. Rapid collapse occurs around 22–30 K and 38–49 K. The collapse continues after these two stages but significantly slower. Above about 70 K, the decrease is linear with increasing temperature. The total thinning for pure H_2O between 22 and 120 K is 12 %. The CO_2 ice thickness decreases linearly with temperature over the studied temperature range. The thermal collapse for pure CO_2 ice between 20 and 50 K is 11 %. For H_2O-CO_2 (4:1), the thermal collapse can only be derived for ice grown at 40 K. The thickness decreases linearly between 40 and 50 K. After this, the thickness reaches a plateau and at 80 K, the total thermal collapse from 40 K is 4 %. At around 83 K, the thickness drops rapidly, likely due to loss of the CO_2.

Fig. 3.8 shows the total thermal collapse (in %) for pure H_2O and CO_2 ice deposited at different temperatures. For CO_2 ice, the collapse is linearly smaller for samples grown at higher temperatures, consistent with the thermal collapse in Fig. 3.7. For H_2O samples grown at 17, 22 and 30 K, the total collapse decreases linearly with growth temperature. For H_2O ice grown at 40 K, the thermal collapse is larger than for the adjacent points. From 40 K onwards, the magnitude of the collapse exhibits a near linear decrease with temperature. The larger total thermal collapse for H_2O ice grown at 40 K is consistent with the low initial density deduced from the sample growth rates in Fig. 3.5.

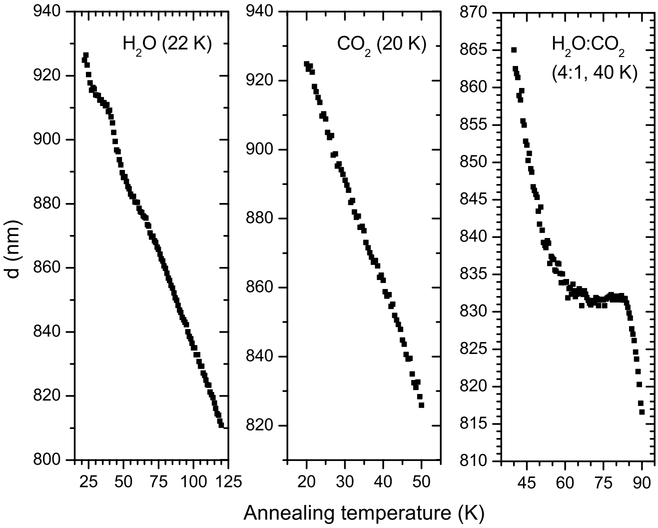

Figure 3.7 – Decrease of thickness upon thermal annealing of H_2O, CO_2, and H_2O-CO_2 (4:1) ices deposited at 22, 20 and 40 K. Note that the thickness and temperature ranges are not the equal.

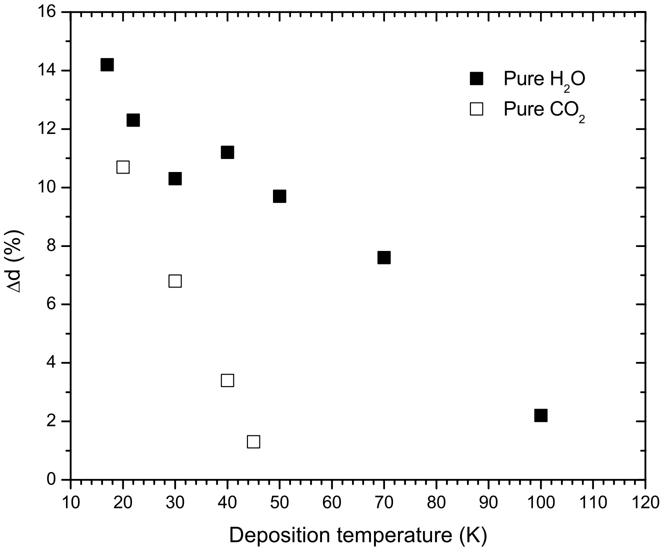

Figure 3.8 – Total decrease of thickness (in %) of H_2O and CO_2 ices grown at different temperatures. The collapse for H_2O and CO_2 is calculated until 120 and 50 K, respectively.

Table 3.3 – Density and surface coverage for background deposited pure H_2O and CO_2 ices, as well as the H_2O-CO_2 (4:1) binary mixture.

Sample	ρ_n [molecules cm^{-3}]	ρ g cm^{-3}	$\rho_{n,xy}$ molec cm^{-2}
H_2O (17 K)	2.5×10^{22}	0.73	0.84×10^{15}
CO_2 (20 K)	1.5×10^{22}	1.09	0.61×10^{15}
H_2O-CO_2 (40 K)	2.1×10^{22}	–	0.75×10^{15}

3.3.4 IR spectroscopy

3.3.4.1 Density

We derive the number density (ρ_n, in molecules cm^{-3}) of pure H_2O and CO_2 using Eq. 3.9:

$$\rho_n = \rho_{n,z}^3 = \left(\frac{N}{d \times \rho_{n,xy}}\right)^3 \tag{3.9}$$

where N is the column density (in molecules cm^{-2}) obtained using Eq. 3.8 from the integrated intensity of an IR absorption feature, $\rho_{n,xy}$ is the monolayer coverage (in molecules cm^{-2}), d is the ice thickness (in cm) obtained from the optical interference measurement and $\rho_{n,z}$ is the vertical number density (along the surface normal, in molecules cm^{-1}). While a surface coverage of 1×10^{15} molecules cm^{-2} is typically used for interstellar ice analogs, we assume isotropic density $\rho_{n,z}^2 = \rho_{n,xy}$, *i.e.*, such that the ice density does not depend on the direction.

Table 3.3 gives the densities and adapted surface coverage values for pure H_2O and CO_2 ice, as well as H_2O-CO_2 (4:1) binary ice. For H_2O, we used $\int A\, d\bar{\nu}$ from the bulk OH stretching band (around 3300 cm^{-1}). For CO_2, $\int A\, d\bar{\nu}$ was derived from the ^{13}C=O stretching band (at 2283 cm^{-1}) using a relative ^{13}C (^{13}CO/^{12}CO) abundance of 1.1 %. In the H_2O-CO_2 ice, the molecular environment changes the intrinsic band strengths of the IR features, and those derived for pure ices cannot be used for mixed ice. The density of H_2O-CO_2 (4:1) ice can be derived indirectly using the molecular deposition rate of pure ices (in molecules cm^{-2} s^{-1}), which, assuming a similar sticking coefficient, does not depend on the ice composition. The molecular deposition rates derived for pure H_2O and CO_2 are 9.2 and 4.4×10^{14} molecules cm^{-2} s^{-1}, respectively. The density given for H_2O-CO_2 ice in Table 3.3 is calculated using a deposition rate average of the pure ices (6.8×10^{14} molecules cm^{-2} s^{-1}) and a thickness derived from the interference data.

3.3.4.2 IR spectra of H_2O-CO_2 (4:1) ice

Fig. 3.9 shows the selected IR features in H_2O-CO_2 (4:1) binary ice grown at 16 K and annealed to 140 K. The left panel shows the region covering the CO_2 (ν_1+ν_3) combination and (2ν_2+ν_3) combination/overtone bands as well as the H_2O (ν_3) dangling OH band. The

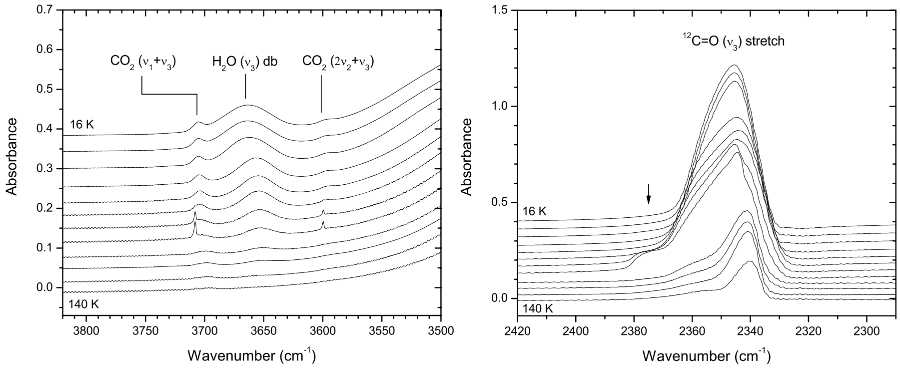

Figure 3.9 – IR spectra of H_2O-CO_2 (4:1) ice around the H_2O (ν_3) dangling OH bond and CO_2 (ν_1+ν_3) combination and (2ν_2+ν_3) combination/overtone bands (left panel), and ^{12}C=O (ν_3) antisymmetric stretching band (right panel). The spectra are recorded at 16, 20, 30, 40, 50, 60, 70, 80, 90, 100, 120 and 140 K. The spectra are offset for clarity.

right panel shows the ^{12}C=O (ν_3) antisymmetric stretching band. Thermal evolution of the ^{12}C=O (ν_3) band shows a clear change in the band profile between 30 and 40 K, as well as between 60 and 90 K. The former is seen as a flattening of the band profile. At 70 and 80 K, the ^{12}C=O (ν_3) feature shows significant substructure, not visible in the low-temperature spectra. In particular, a shoulder appears at around 2375 cm^{-1} indicated by an arrow and the main feature shows a superposed peak around 2345 cm^{-1}. A significant amount of CO_2 remains frozen after the thermal desorption temperature of pure CO_2 ice between 80 and 90 K.

The CO_2 (ν_1+ν_3) combination and (2ν_2+ν_3) combination/overtone modes are visible in the low temperature spectra as broad absorption profiles. At 70 and 80 K, these bands show sharp and narrow profiles, which disappear before 90 K. Particularly the stronger CO_2 (ν_1+ν_3) band remains visible as a broad profile under the sharp feature and persists upon further annealing. The dangling OH band gradually decreases with temperature and is barely visible in the 100 K spectrum.

3.4 Discussion

3.4.1 Refractive index of pure H_2O

The refractive index (n_1) derived for pure H_2O (Fig. 3.5) grows linearly with temperature between 60 and 120 K. Between 17 and 60 K, n_1 first increases with temperature reaching a maximum at 40 K and subsequently decreases towards 60 K. By using the same method (optical interference), Dohnálek et al. (2003) derived n_1 with an overall linear temperature dependence between 22 and 140 K. Because of the small number of data points the non linearity of their data between 22 and 40 K may have been missed. Berland et al. (1995)

report a near linear temperature dependence at deposition temperatures above 35 K. Excluding the non linearity at lower temperatures, our values are in general agreement with those available from the literature. Some variation in the obtained n_1 values is expected due to different experimental conditions, such as deposition pressure (Berland et al. 1995) and the incident angle of the laser beam (Baratta & Palumbo 1998). To our knowledge, this is the first time the refractive index of porous ASW has been studied for such low temperatures, and with a temperature resolution enough to distinguish the non-linearity.

3.4.2 Thermal annealing of pure H_2O

3.4.2.1 Thermal collapse

As we already showed in Bossa et al. (2012), thermal annealing of porous ASW between 20 and 120 K results in a pore collapse accompanied by 12 % thinning of the ice. There the collapse was derived using the linear $n_1(T)$ from (Dohnálek et al. 2003). Ices studied here are grown under identical experimental conditions as those in Bossa et al. (2012). In the present work a number of improvements are implemented. The optical interference is induced by an intensity stabilized laser. Furthermore, the larger angle of incidence of the laser allows for greater sensitivity to changes in the ice thickness. The $n_1(T)$ values used are sample specific at a particular growth temperature. The thermal collapse derived in this work, 12 % for the sample grown at 22 K and annealed to 120 K, is in excellent agreement with the value obtained in Bossa et al. (2012).

3.4.2.2 $I_{hda} \rightarrow I_{lda}$ phase transition at 38-68 K

In our experiments, the interference signal during thermal annealing of pure H_2O shows a consistent discontinuity around 40–50 K, where the signal decreases faster than for adjacent regions. The ice thickness derived from the interference signal and $n_1(T)$ indeed shows a faster thinning between 38 and 49 K, followed by a slow thinning between 49 and 70 K. This temperature region coincides with the phase transition in ASW from high-density form (I_{hda}) to low-density form (I_{lda}), which takes place at 38–68 K (Jenniskens & Blake 1994). The transition allows H_2O molecules to reposition themselves into a more energetically favorable configuration, which intrinsically leads to a less compact lattice structure. This phase transition, expected to occur around 72-78 K based on the hydrogen bond enthalpy, occurs at lowered temperature due to defects in lattice structure (Sciortino et al. 1992, Jenniskens et al. 1995).

The $I_{hda} \rightarrow I_{lda}$ phase transition, however, only describes the change in the intrinsic structure of ASW, disregarding the pores in the ice structure. While the intrinsic density of ASW decreases as a result of the phase transition, the global density may not. In fact, our results suggest that the onset of the phase transition at 38 K triggers enhanced pore collapse manifesting itself as a faster decrease in thickness. Enhanced formation of complex organics demonstrated in vapor deposited ices around the ASW phase transition (Jenniskens & Blake 1994, Schutte 1988), may therefore not be directly due to an intrinsic phase change, but due to a rapid pore collapse triggering premature recombination of radicals. Indeed, slow changes in the chemical composition of these samples is already observed below 38 K and the onset of the phase transition.

Jenniskens et al. (1995) showed that vapor deposition of H_2O below 30 K results in I_{hda}. The total thermal collapse of pure H_2O samples grown at different temperatures shows a distinct behavior for samples deposited at ≤30 K and ≥40 K, respectively (Fig. 3.10). The total thermal collapse (in % of thickness) for both regimes decreases linearly with increasing deposition temperature. However, the values ≥40 K are offset and in general higher than those ≤30 K. Assuming that porosity in the ice decreases gradually with increasing deposition temperature, the discontinuity between the values derived for ≤30 K and ≥40 K is implied to be due to different intrinsic structure of the ice. Extrapolation of the values ≥40 K (I_{lda}) by a linear fit to 30 K gives a total thermal collapse of 12.8 % for a hypothetical case of the I_{lda} with porosity corresponding to ice deposited at 30 K. The total thermal collapse of I_{hda} grown at this temperature is 10.3 %. The difference in the thermal collapse of I_{hda} and I_{lda} normalized for porosity is 19.5 %. The difference in the density of I_{hda} and I_{lda} (1.17 g cm^{-3}, Mishima et al. (1984), and 0.94 g cm^{-3}, Narten et al. (1976), respectively) is strikingly similar, 19.7 %. We conclude that the offset in

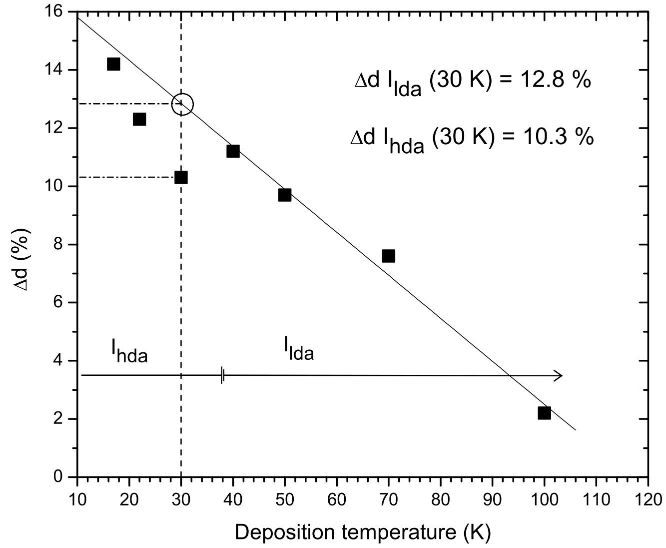

Figure 3.10 – Total thermal collapse of pure H_2O ices grown at different temperatures and annealed to 120 K. The data points at T≥40 K are linearly extrapolated to obtain a hypothetical data point corresponding to I_{lda} ice with porosity consistent with 30 K. The temperature regions dominated by I_{hda} and I_{hda} from annealing experiment (Jenniskens & Blake 1994) are indicated in the figure.

the total thermal collapse for porous ASW grown ≤30 K and ≥40 K is purely due to the different intrinsic density of the morphologies formed in the two regimes. This is also in agreement with the discontinuity observed at 38–49 K upon thermal annealing being related to the $I_{hda} \rightarrow I_{lda}$ phase change.

Through X-ray diffraction, Jenniskens & Blake (1994) observed the intrinsic phase change to occur gradually between 38 and 68 K. In our samples, the fast thickness decrease observed at 38–49 K is followed by a phase of slow thinning until ~70 K. This is consistent with continuing $I_{hda} \rightarrow I_{lda}$ phase change beyond 49 K, where the gradual thinning due to the decrease in porosity is compensated by expanding intrinsic structure. After the phase transition is complete around 70 K, the thickness decrease continues at a slightly faster phase. The enhanced thinning around 38-49 K was not observed in our previous study (Bossa et al. 2012) despite identical ice growth conditions. We presume that the improved conditions in the present work allow to visualize this effect, that must have been just below the detection sensitivity in Bossa et al. (2012).

It is interesting to note that a phase of rapid thinning is also observed at 22–30 K followed by a slower collapse until 38 K (Fig. 3.7). The interpretation of this region, however, is difficult due to experimental constraints. In particular, n_1(T=17 K) is obtained at the base temperature of the cryostat without temperature adjusting and may influence the thickness derived at low temperatures. Experiments at lower temperatures are needed to properly characterize n_1 below 22 K. In the current setting this is not possible. Nevertheless, it is clear that at least some thermal collapse already occurs at these low temperatures.

3.4.3 Density of pure H_2O

The density derived spectroscopically for H_2O ice at 17 K is 0.73 g cm^{-3}, markedly higher than that from the Lorentz-Lorenz relation in the form used in Dohnálek et al. (2003), which gives 0.63 g cm^{-3}. The value derived using the intrinsic band strength of the H_2O (ν_3) stretching mode from Hagen (1981), may be influenced by the spectral differences between ice grown with different morphology. The ices studied in Hagen (1981) are likely to have had lower porosity than the ices studied here, due to a different deposition method; a 5 % error in the intrinsic band strength is enough to explain the difference. Berland et al. (1995) derived a density of 0.68 g cm^{-3} for ice deposited at 35 K and Dohnálek et al. (2003) ~0.62 g cm^{-3} for ice at 22 K. Raut et al. (2007b) derived a density of 0.69 g cm^{-3} for H_2O ice grown through directed deposition (45°) at 30 K.

3.4.4 Residual porosity in annealed H_2O

For porous H_2O ice grown at 17 K the total thermal collapse upon annealing to 120 K is 14 %. Due to the direct inverse correlation between thickness and density[1] the increase in density should be 14 %. Adopting an initial density from the Lorentz-Lorenz relation (0.63 g cm^{-3}) gives a density of 0.72 g cm^{-3} after annealing. This is below the density of ice deposited at 120 K (0.83 g cm^{-3}), implying that initial porosity in the ice is fully destroyed in the annealing process. Fig. 3.11 shows the porosity $1-\rho/\rho_c$ before and after annealing to 120 K for pure H_2O ices deposited at different temperatures. The density

---

[1] $\rho = n/(A \times d)$; assuming negligible desorption (n = constant) and one dimensional collapse ($A \gg d$)

of fully compact ASW (ρ_c) is approximated to be equal to the intrinsic density of I_{lda} (0.94 g cm^{-3}) (Raut et al. 2007a, Westley et al. 1998). It is evident that ice deposited at 120 K has a significant degree of porosity. The residual porosity in samples grown <120 K and annealed to 120 K is about double of that in H_2O deposited at 120 K. It is clear that porous ASW has a "memory" of its original morphology at least throughout the amorphous phase. The ice is still likely to have a significant number of cavities, which makes the global ice density low.

The persistence of porosity upon thermal annealing poses a contradiction to the original approximation, that n_1 (T) is the same for both ice deposited at temperature T, and ice annealed to temperature T. Underestimation of porosity for annealed samples results in overestimation of n_1. This translates to underestimation of ice thickness after annealing and thus overestimation of thermal collapse. Therefore, the values of thermal collapse given in Fig. 3.8 are upper limits. Since porosity in general depends on deposition temperature, the overestimation is likely to be highest for ices deposited at the lowest temperatures.

The presence of cavities throughout the solid phase, beyond crystallization, is consistent with the observation that the amplitude of the fringe pattern during ice desorption, is smaller for ices grown at lower temperature (Fig. 3.6). While the decrease in amplitude may also be due to a change in refractive index, the signal intensity at the constructive interference is a direct indication of loss of photons due to scattering in the ice. Scattering may be more prominent for initially more porous ice if thermal collapse is not able to fully close the pores. Cavities may then remain in the ice throughout the crystalline phase. It has been suggested that scattering may also be due to cracking of the ice (Baragiola 2003) although such effects are more likely for ices that are significantly thicker than studied here (Westley et al. 1998). H_2O ice containing large pores (2-50 nm, *mesoporous* ASW) has been shown to retain a third of the original porosity beyond crystallization (Raut et al. 2007a). Mesoporous ices were obtained through collimated deposition with a large incident angle (77°), known to produce exceptionally porous structures (Stevenson et al. 1999, Kimmel et al. 2001b,a, Dohnálek et al. 2003). These cavities remaining at high temperatures are not visible through IR spectroscopy of the dangling OH bonds, which disappear before crystallization. This has been interpreted as either coalescence of smaller pores into larger pores, preferential destruction of small pores or decrease of surface roughness of the pores (Raut et al. 2007b). Our results support this picture and suggest that omnidirectional background deposition of H_2O – applicable to the vapor deposition in the ISM – possibly results in large pores sustained in the ice upon thermal annealing.

3.4.5 Pure CO_2 ice

The refractive index (n_1) of pure CO_2 ice (Fig. 3.5) grows linearly with temperature until the completion of crystallization at 50 K, after which it decreases. Our results generally agree with those in Satorre et al. (2008), within 2 %. The thermal collapse of CO_2 (Fig. 3.7) proceeds linearly with temperature, with a total collapse of 11 % in thickness for ice deposited at 20 K. Satorre et al. (2008) report a linear density correlation with

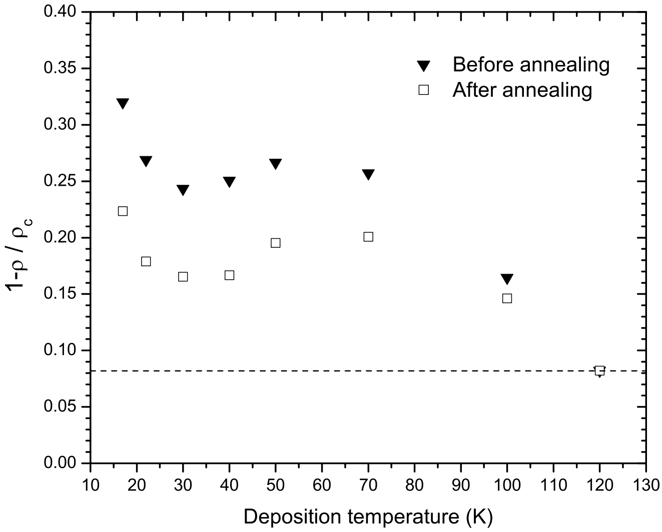

Figure 3.11 – Porosity $1–\rho/\rho_c$ derived for the porous ASW ices annealed to 120 K. ρ values are derived from the Lorentz-Lorenz equation taking into account the thermal collapse. For ρ_c=0.94 g cm^{-3} (Narten et al. 1976) is used.

temperature, consistent with our thermal collapse. We derive a density of 1.09 g cm^{-3} for CO_2 ice grown at 20 K, in excellent agreement with Satorre et al. (2008) (1.06 g cm^{-3}).

3.4.6 H_2O-CO_2 binary ice

The refractive indices measured for H_2O-CO_2 ice (Fig. 3.5) resemble those of pure CO_2 ice. The values at 20 and 30 K, however, differ from the trend observed for pure CO_2 ice. The same is true for the density inferred from the deposition rate, which is much lower for 20 and 30 K compared to 40 K and above. A qualitative difference is also observed in the interference signal during annealing of H_2O-CO_2 ices deposited at different temperatures (Fig. 3.6). For H_2O-CO_2 binary ice grown at 20 and 30 K, the interference signal decreases beyond the theoretical minimum set by total destructive interference, and returns only upon ice evaporation. The total loss of photons can only result from severe scattering in the ice and suggests that a H_2O-CO_2 binary ice deposited at temperatures at ≤30 K is qualitatively different to that deposited at higher temperatures. The transition temperature coincides with that of the onset of the $I_{hda} \rightarrow I_{lda}$ phase transition in amorphous ASW. A similar loss of signal is not observed for H_2O-CO_2 binary ice with a larger mixing ratio (9:1), which indicates that the effect is determined by the relative amount of CO_2 in the binary ice. It has been shown that co-deposition of compact (non-porous) Ar:H_2O ice at 5 K, followed by thermal cycling results in porous ice (Givan et al. 1996). Possible migration/compaction of the CO_2 component in the H_2O-CO_2 ice may leave the ice surface rough and causing optical scattering. At lower mixing ratio, this effect may be less effective or result in finer roughness, not probed by the laser. It is interesting to note that the difference in density between 30 and 40 K is much more dramatic for H_2O-CO_2 binary ice than for either of the pure ices, emphasizing the structural difference in also the mixed ice between the temperature regimes ≤30 K and ≥40 K. The thermal evolution of the $^{12}C{=}O$ (ν_3) IR feature in H_2O-CO_2 ice deposited at 16 K (Fig. 3.9), indeed shows a change in band profile between 30 and 40 K, although the spectral interpretation of this change is difficult. For pure CO_2, the change in the $^{12}CO_2$ feature upon thermal annealing is seen as narrowing and increasing of the peak intensity (Isokoski et al. in prep.).

For H_2O-CO_2 ice deposited at 40 K, we are able to derive a thermal collapse of 3.9 % (40-80 K), slightly lower than for pure H_2O ice within the same temperature range (5.1 %). However, the optical analysis of two-component ices may be problematic for components with very different refractive indices (Raut et al. 2007b). For H_2O and CO_2 the difference in n_1 is 0.7–8 % depending on the temperature, and more elaborate optical analysis is necessary to reliably quantify the thermal collapse. We are currently conducting a more detailed analysis of mixed ices by employing Bruggemans and Maxwell-Garnett rules (Born & Wolf 1975) in the interference, which may account for the presence of CO_2 and vacuum enclosures in the H_2O ice in a more precise way (Bossa et al. in prep.).

3.4.7 CO_2 segregation

Segregation of ice components is typical for thermally annealed ices containing H_2O and CO_2. Segregation of CO_2 occurs around 60–90 K before its bulk desorption and is evidenced by the appearance of IR features characteristic of pure CO_2 ice (Hodyss et al. 2008, Öberg et al. 2009a). The emergence of several spectral features attributed to pure CO_2 is found at temperatures of 70 and 80 K. In particular, the $^{12}C{=}O$ (ν_3) feature shows significant substructure, and a prominent shoulder at 2375 cm^{-1} is only visible in the 70 and 80 K spectra. This shoulder has been shown to appear in IR spectra of pure CO_2 ice, recorded at an angle that is not normal to the ice surface (Baratta et al. 2000). The CO_2 (ν_1+ν_3) combination and ($2\nu_2$+ν_3) combination/overtone bands are sensitive to the matrix environment (Keane et al. 2001). While these bands are visible for the H_2O-CO_2 ice at all temperatures, at 70 and 80 K sharp peaks appear at 3708 and 3600 cm^{-1}, characteristic for pure CO_2 ice (Sandford & Allamandola 1990), and consistent with a segregation process in which H_2O and CO_2 separate.

Hodyss et al. (2008) studied segregation in compact H_2O-CO_2 binary ices (4:1 and 9:1) through IR spectroscopy. Their samples were grown through directed deposition and therefore have a more compact structure than our samples. The extent of segregation was determined through quantification of the pure (crystalline) CO_2 fraction by fitting the $^{13}CO_2$ (ν_3) band as a sum of two line profiles centered at 2282 and 2277 cm^{-1}, corresponding to a pure CO_2 component and a component where CO_2 is isolated in the H_2O matrix, respectively:

$$\text{Pure CO}_2\text{ fraction} = \frac{\int A(2282\ \mathrm{cm}^{-1})\, d\bar{\nu}}{\int A(2277\ \mathrm{cm}^{-1})\, d\bar{\nu} + \int A(2282\ \mathrm{cm}^{-1})\, d\bar{\nu}}$$

They found that the amount of pure CO_2 depends strongly on the temperature at which the ice has been grown. While for ice grown at 70 K the crystalline fraction can be as high as 90 %, for ices grown below 60 K, and subsequently annealed to 70 K, the crystalline fraction remains below 40 %. Particularly interesting is, that for ices grown between 15 and 50 K, the resulting crystalline fraction is larger for lower growth temperatures. This result may imply a link between initial morphology (porosity) and the extent of segregation. As our ices are inherently more porous than those studied by Hodyss et al. (2008), we attempt to confirm this link.

The $^{13}CO_2$ (ν_3) feature does not depend on the angle of the IR beam (Baratta et al. 2000) and can therefore be compared with the results of Hodyss et al. (2008). Fig. 3.12 shows the pure CO_2 fraction in H_2O-CO_2 (4:1) ice deposited at <20 K upon annealing to 120 K for porous ice studied here and compact ice from Hodyss et al. (2008). For the spectra ≥70 K, the positions of Gaussians were fixed to those used in Hodyss et al. (2008) while the other parameters were allowed to vary freely. For the spectra ≤60 K, the use of only two fixed-position Gaussians does not result in a good fit, and we add an additional feature around 2279 cm^{-1}. The position of the two Gaussians remains fixed during the fitting. The width of these features is fixed to those found at 70 K while all the parameters of the 2279 cm^{-1} feature are allowed to vary freely. For porous H_2O, we derive a maximum pure CO_2 fraction of 70 %, occurring at 80 K. This is significantly higher than found by Hodyss et al. (2008) (40 %). Fayolle et al. (2011) showed that segregation in H_2O-CO_2 is influenced by the mixing ratio as well as the ice thickness. We conclude therefore that porosity also influences the segregation process: In ice grown at temperatures below the onset of CO_2 segregation, greater porosity results in more effective segregation upon annealing.

Fig. 3.12 shows a considerable amount of pure CO_2 ice even at low temperature, before the onset of segregation. This was not reported by Hodyss et al. (2008). Below 60 K the $^{13}CO_2$ (ν_3) feature is not adequately fitted with two Gaussians, and the additional feature required at 2279 cm^{-1} may contribute to the intensity of the 2282 cm^{-1} feature and consequently to the pure CO_2 fraction. While the interpretation of the low-temperature feature is beyond the scope of this work, the comparison of spectral differences between compact and porous ices may be beneficial for understanding the morphology in mixed ices.

Hodyss et al. (2008) found that for binary ice deposited at the temperatures of CO_2 segregation, a much larger pure fraction results. This result is consistent with our interpretation of the desorption fringe pattern. For H_2O-CO_2 ice deposited at 60 K, before onset of the segregation, the amplitude of the desorption fringe pattern is large compared to that for 80 K (Fig. 3.6). At 80 K, segregation occurs during deposition allowing large pockets of pure CO_2 to form (Öberg et al. 2009a). These pockets may be large enough to cause optical inhomogeneities and scattering of our interference laser.

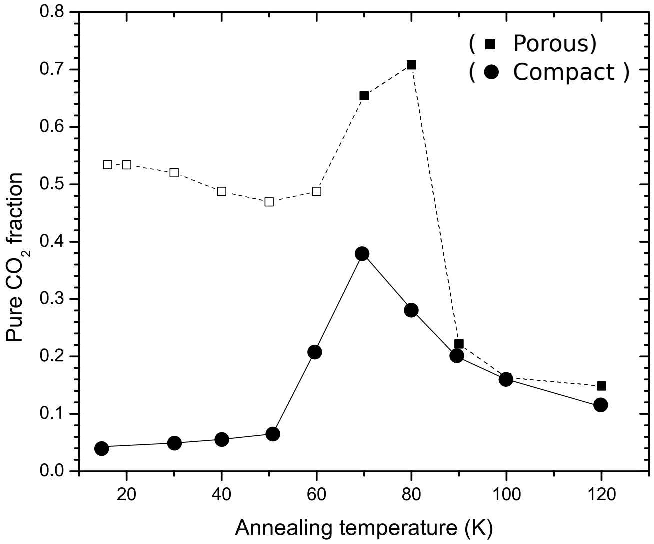

Figure 3.12 – Pure CO_2 ice fraction in H_2O-CO_2 ice upon thermal annealing for porous ice (squares) and compact ice (circles, from (Hodyss et al. 2008)). The data points for porous ice are derived by fitting the $^{13}CO_2$ (ν_3) feature with two-component Gaussian fit (filled squares) and with three-component Gaussian fit (open squares).

3.5 Summary and conclusions

We have studied the morphology of porous amorphous H_2O, CO_2, and H_2O-CO_2 ices in the astronomically relevant temperature range 17-200 K. Using laser optical interference together with FTIR spectroscopy, we have found the following:

1. Porous ASW (H_2O) undergoes a gradual thermal collapse throughout the amorphous regime. A total thinning of 12 % is derived between 22 and 120 K. This value is an upper limit.

2. The intrinsic $I_{hda} \rightarrow I_{lda}$ phase transition in ASW is seen as an enhanced decrease in thickness at 38–49 K and appears to accelerate the pore collapse. The thinning of porous H_2O between 38 and 70 K appears as a combined effect of pore collapse and lattice expansion due to this phase transition.

3. H_2O grown in a porous way is not fully compacted by thermal annealing. Depending on the growth temperature, the residual porosity after annealing to 120 K is around 20 %. Large cavities remain in the ice throughout the solid phase, not observable though infrared spectroscopy.

4. The porous structure of H_2O is retained in the presence of CO_2 at ≤30 K. The morphology and changes upon thermal annealing are highly dependent on the initial

ice porosity and mixing ratio. Significant morphological changes occur around the $I_{hda} \rightarrow I_{lda}$ phase transition, which are not related to CO_2 segregation occurring at higher temperatures.

5. A high initial porosity leads to a higher extent of CO_2 segregation at 70–80 K.

The morphology of the H_2O containing ices is dominated by both the intrinsic structure of ASW as well as porosity. Both influence the dynamics in low-temperature ices, and may have significant consequences for the solid state chemistry in interstellar ices loaded with reactive intermediates.

The initial porosity of the ice determines its structure throughout the solid phase until ice evaporation. H_2O rich ices formed by vapor deposition on cold interstellar dust grains may contain large cavities that persist over a large temperature range, and affect the catalytic potential of the ice as well as the trapping of gases.

The assumption that ASW in space is compact is likely not fully correct. Energetic processing and thermal annealing decrease the porosity, but the non-detection of the dangling OH bond cannot be taken as a proof that interstellar ice is poreless.

CO_2 is the most common impurity in astronomical H_2O ice, with relative abundances varying from 15 to 40 %. For mixed ices, growth conditions influence the morphology, which at higher temperatures affects astronomically relevant processes such as segregation.